Research article

Deep-learning-based 3D super-resolution CT radiomics model: Predict the possibility of the micropapillary/solid component of lung adenocarcinoma

Xiaowei Xing [a], Liangping Li [b], Mingxia Sun [b], Jiahu Yang [b], Xinhai Zhu [c], Fang Peng [d], Jianzong Du [e,1], Yue Feng [a,*,1]

[a] *Cancer Center, Department of Radiology, Zhejiang Provincial People's Hospital, (Affiliated People's Hospital), Hangzhou Medical College, Hangzhou, Zhejiang, China*
[b] *Department of Radiology, Zhejiang Hospital, Hangzhou, Zhejiang, China*
[c] *Department of Thoracic Surgery, Zhejiang Hospital, Hangzhou, Zhejiang, China*
[d] *Department of Pathology, Zhejiang Hospital, Hangzhou, Zhejiang, China*
[e] *Department of Respiratory Medicine, Zhejiang Hospital, Hangzhou, Zhejiang, China*

ARTICLE INFO

ABSTRACT

Objective: Invasive lung adenocarcinoma (ILA) with micropapillary (MPP)/solid (SOL) components has a poor prognosis. Preoperative identification is essential for decision-making for subsequent treatment. This study aims to construct and evaluate a super-resolution (SR) enhanced radiomics model designed to predict the presence of MPP/SOL components preoperatively to provide more accurate and individualized treatment planning.
Methods: Between March 2018 and November 2023, patients who underwent curative intent ILA resection were included in the study. We implemented a deep transfer learning network on CT images to improve their resolution, resulting in the acquisition of preoperative super-resolution CT (SR-CT) images. Models were developed using radiomic features extracted from CT and SR-CT images. These models employed a range of classifiers, including Logistic Regression (LR), Support Vector Machines (SVM), k-Nearest Neighbors (KNN), Random Forest, Extra Trees, Extreme Gradient Boosting (XGBoost), Light Gradient Boosting Machine (LightGBM), and Multilayer Perceptron (MLP). The diagnostic performance of the models was assessed by measuring the area under the curve (AUC).
Result: A total of 245 patients were recruited, of which 109 (44.5 %) were diagnosed with ILA with MPP/SOL components. In the analysis of CT images, the SVM model exhibited outstanding effectiveness, recording AUC scores of 0.864 in the training group and 0.761 in the testing group. When this SVM approach was used to develop a radiomics model with SR-CT images, it recorded AUCs of 0.904 in the training and 0.819 in the test cohorts. The calibration curves indicated a high goodness of fit, while decision curve analysis (DCA) highlighted the model's clinical utility.
Conclusion: The study successfully constructed and evaluated a deep learning (DL)-enhanced SR-CT radiomics model. This model outperformed conventional CT radiomics models in predicting MPP/SOL patterns in ILA. Continued research and broader validation are necessary to

* Corresponding author.
E-mail addresses: pocofan@126.com (X. Xing), Liliangping7@163.com (L. Li), sunmingxia5019@163.com (M. Sun), jhtc6668@163.com (J. Yang), zxh.cool@163.com (X. Zhu), pengfang999@139.com (F. Peng), djzdjz@163.com (J. Du), fengyue1974@gmail.com (Y. Feng).
[1] Yue Feng and Jianzong Du contributed equally to this work and shared the first authorship.

fully harness and refine the clinical potential of radiomics when combined with SR reconstruction technology.

1. Introduction

Lung cancer remains the foremost cause of cancer-related deaths worldwide. Lung adenocarcinoma, which is the most common histological subtype, accounts for nearly half of all lung cancer cases [1]. This subtype of lung cancer is characterized by significant heterogeneity in terms of molecular features, pathological presentation, prognostic outcomes, and treatment approaches. The International Association for the Study of Lung Cancer (IASLC), the American Thoracic Society (ATS), and the European Respiratory Society (ERS) have collaborated to develop and publish a revised histological classification system for lung adenocarcinoma, acknowledging its heterogeneous nature [2]. The updated classification provides a framework for prognostic stratification based on histological patterns. The classification system distinguishes lepidic, papillary, acinar, micropapillary (MPP), and solid (SOL) patterns, which are predominant invasive lung adenocarcinoma (ILA) subtypes. It is common for ILA tissue to exhibit a combination of these subtypes within a single patient [3,4].

Within the spectrum of ILA subtypes, MPP and SOL patterns are closely associated with a poorer prognosis. These particular subtypes correlate with increased rates of recurrence and metastasis in ILA [5–7]. Even if the proportion of MPP/SOL is less than 5 % of ILA tissue, patients still face a significantly increased risk of recurrence or metastasis after surgery [8–12]. This critical insight indicates the potential need for revising treatment approaches. Specifically, for those patients undergoing conservative resection for lung cancer, the existence of MPP/SOL subtypes is recognized as an independent prognostic factor for local recurrence [13,14]. Consequently, precisely identifying micropapillary (MPP) and solid (SOL) components in lung adenocarcinoma before surgery plays a vital role in determining the most effective treatment approach. However, the challenge persists, as preoperative histological evaluations (like CT-guided percutaneous biopsies) often fall short of fully characterizing the tumor's heterogeneity [15,16]. In light of these limitations, preoperative CT imaging assessment may provide a more inclusive appraisal of the patient risk and thus inform subsequent treatment decisions or follow-up protocols.

As an innovative approach, radiomics enables non-invasive quantification of tumor heterogeneity by analyzing a wide range of advanced quantitative features extracted from medical imaging data. This methodology comprehensively examines the radiological attributes and spatial arrangement within tumor tissues [17], allowing for a comprehensive and quantitative evaluation of tumor heterogeneity [18]. Studies have demonstrated that radiomics can improve diagnostic precision and prognostic forecasting by revealing disease characteristics that are difficult to capture with traditional imaging. This advancement holds promise for refining patient management and clinical decision-making processes [19,20]. It has shown its unique value in evaluating lung adenocarcinoma [21]. Recent research has demonstrated that employing radiomics on CT scans, which involves extracting complex quantitative features, provides a non-invasive method for forecasting MPP/SOL patterns in lung adenocarcinoma [22,23]. Nonetheless, radiomics analysis faces challenges due to current medical imaging technology limitations, such as non-uniform spatial resolution and restricted voxel data, which can compromise the accuracy of the extracted radiomic features [24]. Integrating images with superior resolution during the model development process is crucial to addressing these challenges and improving the stability and dependability of radiomics models.

Super-resolution (SR) techniques seek to improve the spatial detail of digital imagery by generating high-resolution versions from lower-resolution source images. This field has seen considerable advancements since it was first proposed in the 1980s [25]. The integration of deep learning (DL) technologies has significantly propelled the effectiveness of SR techniques in the realm of medical imaging [26]. According to Park and colleagues, DL-driven CT slice de-thickening technology can markedly improve the effectiveness of computer-aided detection (CAD) systems in identifying subsolid pulmonary nodules [27]. SR technology exhibits remarkable stability and reliability in processing images with varied spatial gradients. Moreover, the radiomic features derived from SR-enhanced images have also shown significant consistency and robustness [24]. Even so, DL-enhanced SR technology within radiomics, especially for identifying of radiomic biomarkers for clinical use, remains relatively rare [28]. This research seeks to create and validate a radiomics model enhanced by SR technology. The model's objective is to forecast the presence of MPP/SOL components before surgery, enabling the implementation of more accurate and tailored treatment approaches.

2. Material and methods

This study was retrospective.

2.1. Patients

This research was conducted in full compliance with the ethical guidelines outlined in the Declaration of Helsinki (2013 revision). The Human Research and Ethics Committee of Zhejiang Hospital approved this study protocol (approval number 2023-37K). Given the study's retrospective design, the need for informed consent was waived. The study population comprises patients diagnosed with lung adenocarcinoma, as confirmed by pathological examination, at our institution's two centers between March 2018 and November 2023.

The study included patients who met the following criteria: (1)Underwent chest CT scanning within a week before surgical intervention; (2)Had CT images with thin sections (≤1.5 mm) suitable for analysis; (3)Received a pathological confirmation of lung

adenocarcinoma, accompanied by a comprehensive pathology report detailing the subtypes; (4) Had not previously received chemotherapy or radiotherapy; (5) Had clinical records gathered within a week prior to the surgery; (6)Were diagnosed with tumors not exceeding stage II. Patients were excluded from the study if they: (1) Exhibited multiple focal lesions; (2) Underwent biopsy to collect tissue samples rather than surgical removal; (3)Were diagnosed with additional malignant tumors; (4)Had undergone radiotherapy or chemotherapy before CT scanning; (5)Were identified as having microinvasive adenocarcinoma. Fig. 1 illustrates the specific inclusion and exclusion criteria and the patient recruitment process.

Patient information, including demographic data, laboratory test results, and clinical characteristics, was extracted from the electronic medical records system. The gathered clinical data included a variety of metrics and details: Demographic attributes such as gender and age; physical dimensions like height, weight, Body Mass Index (BMI), and body surface area (BSA); details concerning smoking habits, including smoking status, years of smoking, and daily cigarette intake; and a range of tumor markers and biomarkers. These markers included Cytokeratin fragment 19 (CYFRA 21-1), Thyroglobulin (TG), Alpha-fetoprotein (AFP), Carcinoembryonic antigen (CEA), Neuron-specific enolase (NSE), various Carbohydrate antigens (CA125, CA15-3, CA19-9, CA242, CA50, CA72-4), and the Squamous cell carcinoma antigen (SCC).

2.2. Pathological evaluation

All tissue samples underwent neutral formalin fixation and paraffin embedding. These samples were then cut into 4-μm thick sections and stained with hematoxylin and eosin (H&E). Two pathologists collaboratively re-evaluated the slides using a multi-headed microscope. Any discrepancies in their assessments were resolved through mutual discussion. ILA histological subtypes were classified according to the multidisciplinary guidelines established by IASLC, ATS, and ERS [2]. Each histological subtype was quantified using 5 % increments. In the specific case of the micropapillary (MPP) and solid (SOL) subtypes, when their combined component comprised less than 5 % of the total tumor volume, the pathologists provided a more precise measurement using 1 % intervals. Tumors were categorized as having an absent MPP/SOL pattern if these components comprised less than 1 % of the total tumor. The participants in the study were categorized into two groups depending on whether they exhibited an MPP/SOL growth pattern: one group consisted of individuals with ILA but without MPP/SOL components, whereas the other group comprised individuals with ILA that featured components of MPP/SOL.

2.3. Image acquisition

Chest CT images were acquired with six multi-row spiral CT scanners (SIEMENS SOMATOM Force; SIEMENS SOMATOM Definition; GE MEDICAL SYSTEMS Revolution; GE MEDICAL SYSTEMS CT 540; UNITED CT 510; NeuCT Extra 2) at two centers. The CT scanning parameters were configured as follows: detector collimation,1–1.5 mm; field of view: 20–38 cm; beam pitch, 0.800 to 1.5; beam width, 10–40 mm; gantry speed, 0.5 or 0.8 s per rotation; 100–130 kV; 47–351 mA; reconstruction interval, 0.39–0.6 mm; matrix, 512×512, and soft-tissue kernel. All imaging was conducted with patients lying supine at full inspiration, spanning from the thoracic inlet down to the base of the lungs. The CT data were retrieved from the Picture Archiving and Communication System
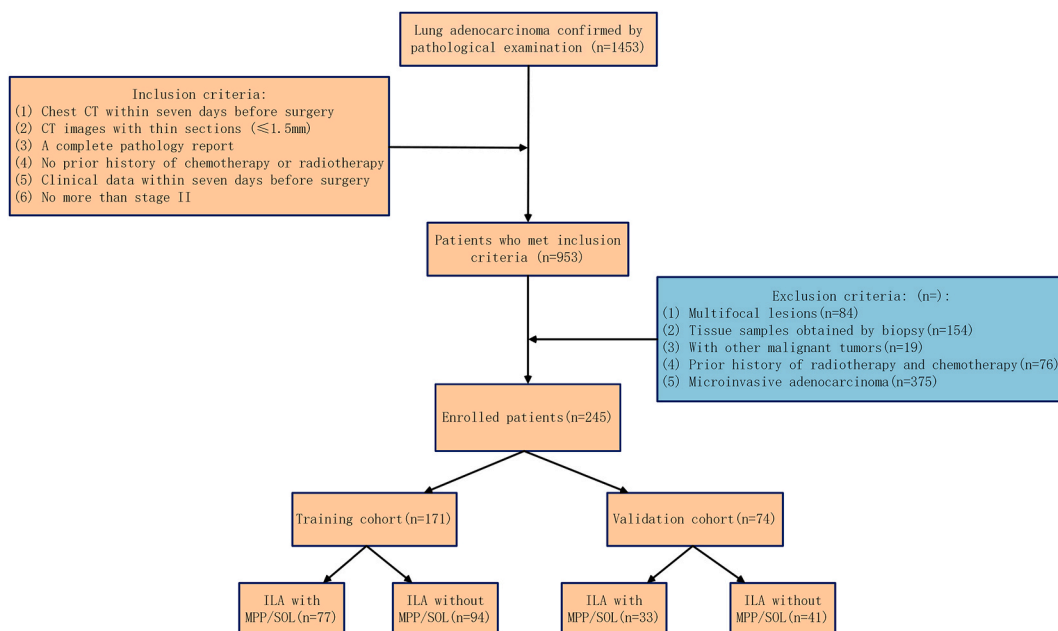

Fig. 1. Flow chart of the patient recruitment process.

(PACS).

2.4. Data preprocessing

The CT images underwent preprocessing steps to improve the consistency of feature extraction and minimize the influence of varying image acquisition parameters on analytical outcomes. Z-Score normalization was applied to the data. Linear interpolation was used to resample the image voxels, uniformly adjusting them to a standard voxel size of $1 \times 1 \times 1$ mm^3. The images underwent grayscale quantization, discretizing the grayscale values and setting each grayscale interval (bin width) to 25 units [29,30].

2.5. Super-resolution reconstruction

The NSCLC-Radiomics dataset is a publicly available and extensively validated collection of data. It comprises computed tomography (CT) scans from 422 patients diagnosed with non-small cell lung cancer (NSCLC). This dataset is accessible through The Cancer Imaging Archive (TCIA) website (https://www.cancerimagingarchive.net/collection/nsclc-radiomics/). This dataset contains 1,265 imaging series consisting of 52,073 images. For our SR reconstruction study, we carefully chose a subset of CT scan series characterized by their high consistency. This subset included 142 CT scan series, amounting to 17,938 CT images. The CT images in this dataset have a resolution of 512×512 pixels. They feature an in-plane pixel spacing of 0.98 mm and a slice thickness of 3.00 mm. All CT scans in this subset were reconstructed using the B19f convolution kernel. In the preprocessing stage of our super-resolution reconstruction workflow, the initial step involved denoising the original high-resolution CT (HRCT) images, known as RAW CT, and eliminating any artifacts. The noise reduction method we utilized is Non-Local Means Denoising [31]. This method reduces noise by comparing the similarity between small areas around each pixel and other regions within the image while preserving the details and structure of the image. Regarding parameter settings, the search window size is 21×21 pixels, and the similarity window is 11×11 pixels. These parameters have been carefully selected to optimize the denoising effect and prevent excessive smoothing of image details. Artifact removal is achieved using an adaptive threshold technique, which identifies brightness anomalies in local areas of the image caused by various reasons [32]. We apply slight Gaussian blurring for local smoothing for these identified abnormal areas, with a Gaussian kernel standard deviation set at 1.5. This step helps mitigate artifacts' impact on the final image quality.
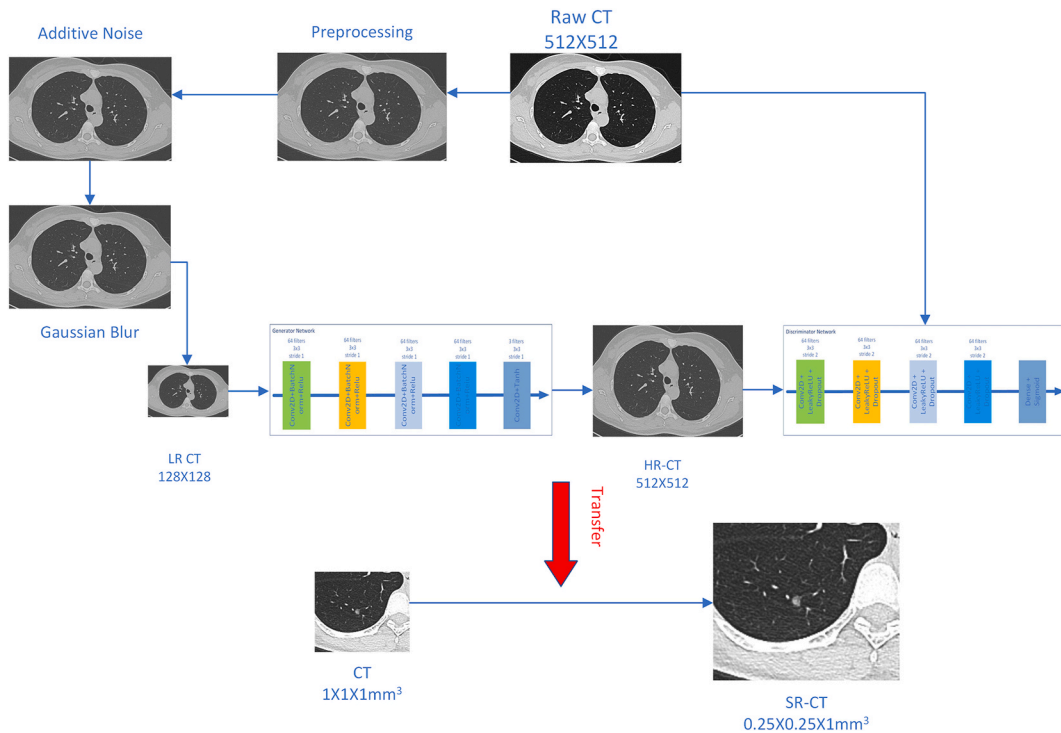

Fig. 2a. Depicts the process of using transfer learning to achieve super-resolution reconstruction of SR-CT images. Fig. 2a: Initially, high-resolution CT scans (RAW-CT) undergo a preprocessing step, which includes the removal of noise and artifacts, as well as the normalization of intensity values. These images are then processed with Gaussian white noise and Gaussian blur, effectively reducing the resolution in the plane orthogonal to the imaging plane by a factor of four, resulting in down sampled, low-resolution CT images (LR-CT). These LR-CT images and synthetic high-resolution CT (HR-CT) counterparts are employed to train a compact parallel generative adversarial network (GAN). Upon successful training, this GAN model is applied to actual patient CT images via transfer learning, enhancing their spatial resolution. As a result, the original pixel volume of $1 \times 1 \times 1$ mm^3 is refined to a higher resolution of $0.25 \times 0.25 \times 1$mm^3, thereby generating the corresponding super-resolution CT images (SR-CT).

Then, we normalized the intensity values across all images to achieve a consistent scale, which is essential for uniformity in the later processing stages. To normalize the intensity values in our images, we utilized a Min-Max Normalization method [33,34], which adjusts the range of the original image data to a standard scale of [0, 1]. The normalization equation is expressed as follows:

$$Inormalized = \frac{I - Imin}{Imax - Imin}$$

Inormalized is the normalized pixel intensity. *I* is the pixel intensity in the original image. *Imin* represents the lowest pixel intensity in the original image, while *Imax* denotes the highest pixel intensity.

This normalization method effectively standardizes the pixel intensities across all images, eliminating variations due to different scanning parameters or devices. Thus, it ensures consistency and comparability of the image data during the super-resolution reconstruction process.

Moreover, we subjected the images to Gaussian white noise and Gaussian blur, intentionally downgrading the resolution to one-quarter of the original along the X and Y axes, thereby generating low-resolution CT images (LR-CT) for the super-resolution process.

We combined generative adversarial network (GAN) and deep transfer learning network in our super-resolution reconstruction [28]. The objective is to transform low-resolution CT images into high-resolution versions, thereby improving spatial resolution.

The 3D SR reconstruction method employs a Generative Adversarial Network (GAN) as its fundamental architecture. GANs are a deep learning model consisting of a generator network and a discriminator network [35]. The generator accepts low-resolution images (128×128) as input and processes them through multiple convolutional layers (Conv2D) with batch normalization (BatchNorm) and ReLU activation functions to extract image features. In the final layer of the generator, the Tanh activation function is used to generate high-resolution images (512×512). The discriminator accepts high-resolution or generated images (512×512) as input and uses multiple convolutional layers (Conv2D) with LeakyReLU activation functions and Dropout layers to determine the authenticity of the images. Finally, the discriminator uses a Sigmoid activation function to output a binary classification (natural or generated). These two networks undergo training in an adversarial manner. The generator aims to create images that can deceive the discriminator, while the discriminator seeks to accurately distinguish between authentic and generated images. This adversarial training process allows the generator network to learn the relationship between low-resolution and high-resolution images effectively. The result of this training is a GAN model. The method of CT image super-resolution reconstruction using generative adversarial networks is illustrated in Fig. 2a.

Using the trained GAN model, low-resolution CT images can be converted into high-resolution images, significantly enhancing their spatial resolution. This process includes three main steps:

1. Segment the input image: The original CT image is segmented into 128×128 patches, each serving as an input.
2. Create high-resolution images: The generator inputs each low-resolution patch measuring 128×128 pixels, producing a corresponding high-resolution image of 512×512 pixels.
3. Combine high-resolution images: All generated high-resolution patches are merged according to their original positions to reconstruct the complete high-resolution CT image.

This approach optimized the voxel size, refining it from the original dimensions of $1 \times 1 \times 1mm^3$ to a more detailed resolution of $0.25 \times 0.25 \times 1mm^3$. This enhancement step resulted in super-resolution CT (SR-CT) images via SR reconstruction, exemplified in Fig. 2b. The quality evaluation of the SR-CT images was performed using two metrics: the Structural Similarity Index (SSIM) and the Normalized Root Mean Square Error (NRMSE) [36]. The SSIM achieved a high score of 0.980, and the NRMSE registered at a low 0.636 %, signifying that the resolution enhancement was substantial. Yet, alterations to the image structure and intensity remained minimal.

2.6. Image segmentation and feature extraction

For each patient, a radiologist with over six years of experience will manually segment both the CT and SR-CT images using ITK-SNAP software (version 3.8.0, available at www.itksnap.org). During the contouring process, the radiologist will carefully exclude areas of necrosis, calcification, cavities, vasculature, and bronchial structures. A senior radiologist with 26 years of professional

Fig. 2b. Original CT images and super-resolution reconstructed CT images (SR-CT). With the increased resolution, SR-CT images are visually almost indistinguishable from the original CT images, yet they exhibit less blurriness, finer texture details, and sharper edges.

experience will review and validate all lesion delineations. Any disagreements will be resolved thoroughly. The regions of interest (ROI) identified will be saved in NIfTI (NII) format and prepared for subsequent analysis.

All radiomics features are extracted using an in-house feature analysis program implemented in Pyradiomics (version 2.2.0, available at http://pyradiomics.readthedocs.io). The workflow for radiomics feature extraction and model construction is depicted in Fig. 3. The types of features analyzed encompass first order, shape, and various texture matrices such as gray-level co-occurrence matrix (GLCM), gray-level size zone matrix (GLSZM), gray-level run length matrix (GLRLM), gray-level dependence matrix (GLDM), and neighboring gray tone difference matrix (NGTDM). The transformations used encompass logarithmic, wavelet, local binary pattern (LBP), exponential, square, square root, and gradient methods. Apart from shape-based characteristics, all radiomic features incorporate these extraction types with designated transformation techniques. Feature selection is conducted on the training cohort. Radiomic features are screened using the Mann-Whitney *U* test, with only those yielding a p-value below 0.05 being retained for further analysis. Features exhibiting high redundancy were analyzed using the Pearson correlation coefficient to determine inter-feature correlations. Only one feature was retained from pairs of features with a correlation coefficient greater than 0.9. In our approach to feature filtering, we implemented a greedy recursive elimination strategy to improve the representation of distinct features. Each iteration systematically removes the feature with the highest redundancy in the current set. The dimensionality of the selected features was reduced using the Least Absolute Shrinkage and Selection Operator (LASSO) algorithm. LASSO shrinks all regression coefficients towards zero based on regulation weights λ and precisely sets the coefficients of irrelevant features to zero. To determine the optimal λ value, we used 10-fold cross-validation, choosing the λ that resulted in the minimum cross-validation error. Features that maintained non-zero coefficients after LASSO regularization were incorporated into the regression model fitting, resulting in a combined radiomics signature. Subsequently, a formula based on the weighted sum of the chosen radiomics features was used to compute a radiomics score (rad-score). We conducted LASSO regression modeling using the scikit-learn package in Python.

2.7. Radiomics model construction and model performance evaluation

After completing the Lasso feature selection process, we input the final set of features into various machine learning algorithms to construct the risk model. These algorithms included Logistic Regression (LR), Support Vector Machines (SVM), k-Nearest Neighbors (KNN), Random Forest, Extra Trees, Extreme Gradient Boosting (XGBoost), Light Gradient Boosting Machine (LightGBM), and Multilayer Perceptron (MLP). To establish the final radiomics profile, 10-fold cross-validation was employed. The diagnostic efficacy of the predictive model was assessed by generating the Receiver Operating Characteristic (ROC) curve and determining the Area Under the Curve (AUC) associated with it. The AUC quantitatively measures the model's discriminatory ability. We determined the optimal threshold using this criterion by identifying the point with the maximum Youden index. Based on this threshold, we then analyzed each model's accuracy, sensitivity, and specificity. To further evaluate the precision of the model's predictions, we utilized calibration curves. The fit of these curves illustrates the agreement between predicted probabilities and observed outcomes. A non-significant result from the statistical test of the calibration curve indicates good model calibration. Furthermore, to assess the clinical utility of the model, we employed Decision Curve Analysis (DCA). DCA allows us to quantify the model's benefits to clinical decision-making by calculating the net benefit across various threshold probabilities. This approach aids clinicians in discerning the net improvement the model may offer to patient outcomes when applied at different probability thresholds.
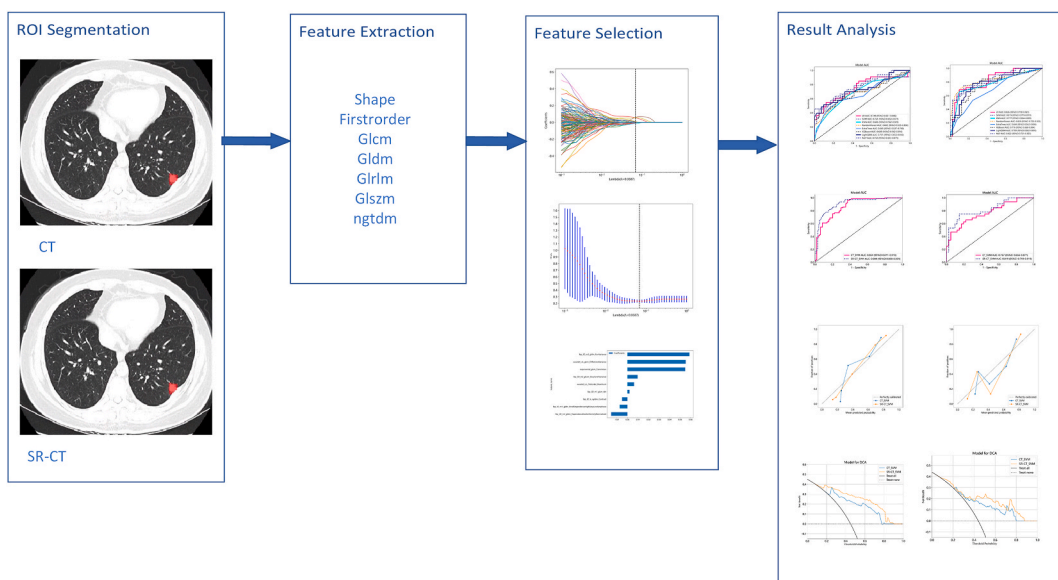

Fig. 3. Workflow for radiomics feature extraction and model construction.

2.8. Statistical analysis

Statistical analyses were conducted using IBM SPSS software (version 22.0, accessible at http://www.ibm.com) and Python (version 3.7.6). To compare continuous variables, we used the Student's t-test or the Mann-Whitney U test. We reported continuous parameters as either the mean ± standard deviation or the median along with the interquartile range. Conversely, we used the χ^2 test to compare categorical features. A p-value less than 0.05 was considered to indicate a statistically significant difference. We implemented bootstrapping with 1,000 iterations to calculate the 95 % confidence intervals (CIs), bolstering the robustness of our findings. To assess the performance of the radiomics models, we implemented 10-fold cross-validation during the training phase. Furthermore, the models underwent validation in an independent test cohort.

3. Results

3.1. Clinical characteristics

The study examined 1453 patients who underwent CT scans for preoperative assessment between March 2018 and November 2023. All patients were diagnosed with lung adenocarcinoma through pathological examination at our institution's two centers. 953 patients met the initial inclusion criteria. Patients were then excluded for the following reasons: (1) multifocal lesions (n = 84); (2) tissue specimens collected through biopsy instead of surgical procedures (n = 154); (3) presence of other malignant tumors (n = 19); (4) prior history of receiving radiotherapy and chemotherapy before the scanning session (n = 76); (5) microinvasive adenocarcinoma (n = 375). The final study cohort comprised 245 patients (118 males and 127 females) who met all inclusion criteria. The average age was 63.53 ± 10.03 years, with a range from 21 to 83 years. In total, 245 pulmonary lesions underwent evaluation. In this study, 109 patients exhibited ILA with MPP/SOL components, whereas 136 patients presented lesions lacking MPP/SOL components. For the purpose of analysis, patients with ILA were divided into two categories: '0' indicating no MPP/SOL components, and '1' signifying their presence. Using stratified randomization with a 7:3 ratio, patients were assigned to a training cohort (171 patients) and a validation cohort (74 patients). Fig. 1 illustrates the patient selection process. Independent sample t-tests, Mann-Whitney U tests, or chi-square tests were used as appropriate to evaluate clinical characteristics across various groups. The initial clinical characteristics of patients within each cohort are displayed in Table 1.

Table 1
Baseline characteristics of patients in cohorts.

feature_name	train-label = 0	train-label = 1	pvalue	test-label = 0	test-label = 1	pvalue
height	1.62 ± 0.08	1.64 ± 0.08	0.32	1.63 ± 0.08	1.66 ± 0.07	0.076
weight	61.93 ± 9.02	62.46 ± 12.49	0.749	61.31 ± 9.32	67.00 ± 9.50	0.012
BMI	23.44 ± 2.58	23.19 ± 3.45	0.598	23.10 ± 3.06	24.35 ± 3.50	0.105
BSA	1.63 ± 0.15	1.68 ± 0.20	0.045	1.62 ± 0.14	1.75 ± 0.17	<0.001
smoke_quantity	4.33 ± 8.22	10.04 ± 13.93	0.001	7.44 ± 12.10	8.52 ± 11.29	0.696
smoking_years	9.20 ± 17.19	15.84 ± 19.03	0.018	10.49 ± 16.73	13.00 ± 17.10	0.527
age	65.00 ± 8.64	61.69 ± 11.43	0.032	61.95 ± 10.22	65.61 ± 9.33	0.116
CYFRA211	2.96 ± 1.53	3.23 ± 3.57	0.499	2.74 ± 1.36	3.06 ± 1.04	0.281
TG	13.16 ± 14.16	12.64 ± 10.54	0.791	15.02 ± 14.37	15.39 ± 12.93	0.909
AFP	3.20 ± 1.41	6.79 ± 29.23	0.237	2.90 ± 1.07	3.24 ± 1.55	0.268
CEA	2.74 ± 1.60	4.62 ± 6.98	0.012	2.51 ± 1.36	6.00 ± 11.72	0.062
NSE	10.91 ± 2.17	11.19 ± 2.66	0.445	11.25 ± 2.20	11.74 ± 2.44	0.365
CA125	10.50 ± 6.36	14.28 ± 15.42	0.032	10.28 ± 4.89	12.82 ± 11.33	0.199
CA153	10.84 ± 4.89	11.85 ± 8.33	0.328	9.27 ± 5.19	12.26 ± 6.72	0.034
CA199	13.90 ± 20.98	42.39 ± 238.33	0.25	12.30 ± 8.70	19.55 ± 19.40	0.036
CA242	6.85 ± 19.56	12.67 ± 50.48	0.305	4.67 ± 2.89	7.94 ± 8.90	0.03
CA50	7.72 ± 9.53	8.85 ± 12.20	0.5	7.58 ± 5.13	54.14 ± 250.63	0.237
CA724	2.70 ± 3.35	4.88 ± 5.97	0.003	3.41 ± 4.62	18.16 ± 63.34	0.141
SCC	0.99 ± 0.49	1.22 ± 0.63	0.011	0.91 ± 0.40	1.62 ± 1.95	0.026
smoke			0.004			0.332
0	71 (75.53)	41 (53.25)		28 (68.29)	18 (54.55)	
1	23 (24.47)	36 (46.75)		13 (31.71)	15 (45.45)	
gender			0.072			0.047
0	58 (61.70)	36 (46.75)		23 (56.10)	10 (30.30)	
1	36 (38.30)	41 (53.25)		18 (43.90)	23 (69.70)	

Clinical data includes gender, age, height, weight, Body Mass Index(BMI), body surface area(BSA), smoking status, daily smoking quantity (smoke_quantity) , years of smoking (smoking_years) , Cytokeratin fragment 19 (CYFRA 21-1), thyroglobulin(TG), alpha-fetoprotein(AFP), carcinoembryonic antigen(CEA), neuron-specific enolase(NSE), carbohydrate antigen 125(CA125), carbohydrate antigen 15-3(CA15-3), carbohydrate antigen 19-9(CA19-9), carbohydrate antigen 242(CA242), carbohydrate antigen 50(CA50), carbohydrate antigen 72-4(CA72-4), and squamous cell carcinoma antigen(SCC).

3.2. Radiomics feature processing and model development

From the lesions on the CT scans, we extracted 1,835 radiomic features, which were segmented into seven groups as follows: 360 first-level, 14 shape, 440 GLCM, 320 GLSZM, 320 GLRLM, 280 GLDM, 100 NGTDM. An identical feature extraction process was carried out on the SR-CT images. Fig. 4 displays the quantity and distribution of all manually crafted features extracted from CT and SR-CT images. Fig. 5a and b displays all the features from both CT and SR-CT, along with their associated p-value outcomes. From the features identified in the final selection step, a radiomics signature was developed. For each patient, a rad-score was computed. This score was calculated as a linear combination of the values of the selected features, with each value multiplied by its corresponding non-zero coefficient. Figs. 6a and b and 7a and b detail the coefficients and Mean Squared Error (MSE) derived from the 10-fold cross-validation. Specifically, Fig. 6a and 7a illustrate the coefficient values for the selected features with non-zero coefficients. Fig. 6b and 7b show MSE of 10-fold cross-validation over the CT data and the SR-CT data. The histogram in Fig. 8a and b depicts the distribution of the rad-score calculated from the selected features over the CT data and the SR-CT data.

The rad-score for CT images is shown as follows:

Rad-score$_{CT}$ = label = 0.4502923976608187 + +0.054967 * exponential_glcm_Correlation −0.005154 * lbp_3D_k_ngtdm_Contrast +0.001985 * lbp_3D_m1_glcm_Idn −0.007332 * lbp_3D_m1_gldm_SmallDependenceHighGrayLevelEmphasis −0.015485 * lbp_3D_m2_gldm_DependenceNonUniformityNormalized +0.058883 * lbp_3D_m2_glrlm_RunVariance +0.009651 * lbp_3D_m2_glszm_GrayLevelVariance +0.006280 * wavelet_LLL_firstorder_Maximum +0.055371 * wavelet_LLL_glcm_DifferenceVariance.

The rad-score for SR-CT images is shown as follows:

Rad-score$_{SR-CT}$ = 0.4502923976608187 + +0.096056 * exponential_glcm_Correlation −0.027199 * exponential_glszm_LargeAreaLowGrayLevelEmphasis −0.005322 * exponential_glszm_SmallAreaLowGrayLevelEmphasis +0.020219 * lbp_3D_k_firstorder_Range +0.013698 * lbp_3D_k_glcm_Correlation −0.011916 * lbp_3D_k_ngtdm_Contrast −0.063876 * lbp_3D_m1_glrlm_GrayLevelVariance −0.040256 * lbp_3D_m1_glrlm_ShortRunLowGrayLevelEmphasis +0.007501 * lbp_3D_m2_glcm_Correlation +0.001263 * lbp_3D_m2_glszm_GrayLevelVariance +0.006528 * lbp_3D_m2_glszm_ZoneEntropy +0.014452 * original_firstorder_10Percentile +0.005678 * square_gldm_LargeDependenceLowGrayLevelEmphasis −0.025791 * square_ngtdm_Coarseness +0.018284 * squareroot_glszm_LargeAreaLowGrayLevelEmphasis +0.029836 * wavelet_HHH_firstorder_Median +0.054224 * wavelet_LLL_firstorder_Maximum.

3.3. Predictive performance of the models

Models were constructed with radiomics features derived from CT images using a range of classifiers such as LR, SVM, KNN, Random Forest, Extra Trees, XGBoost, LightGBM, and MLP, as elaborated in Table 2. Fig. 9 illustrates the AUC for each radiomic model in the test cohort. The SVM model exhibited outstanding results in both the training and test cohorts, with AUC values reaching 0.864 and 0.761, respectively, thereby proving to be the most proficient classifier for the radiomics model. Additionally, when employing SVM to construct a radiomics model using SR-CT images, the AUCs obtained were 0.904 in the training cohort and 0.819 in the test cohort. Fig. 10 illustrates the AUC performance of the radiomics models evaluated on the SR-CT test cohort. Fig. 11a and b compares the AUCs of the SVM models based on radiomic features derived from CT and SR-CT images. Table 3 provides comprehensive results detailing the model's accuracy, sensitivity, and specificity.

The calibration curves exhibited a high level of agreement between the models' predicted probabilities and the actual observed outcomes in both the training and test cohorts, as shown in Fig. 12a and b. Additionally, we conducted DCA for each model to assess
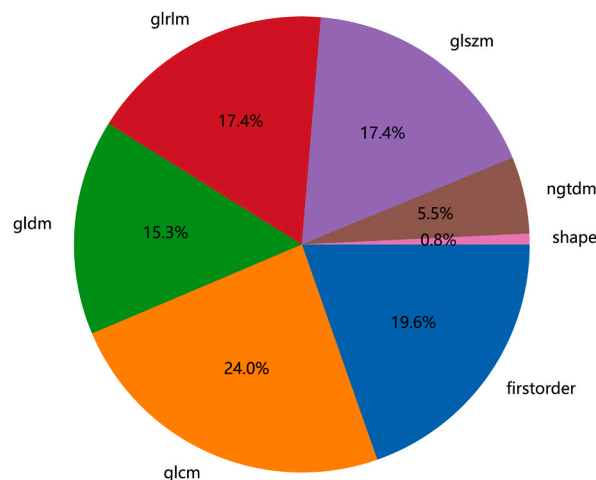

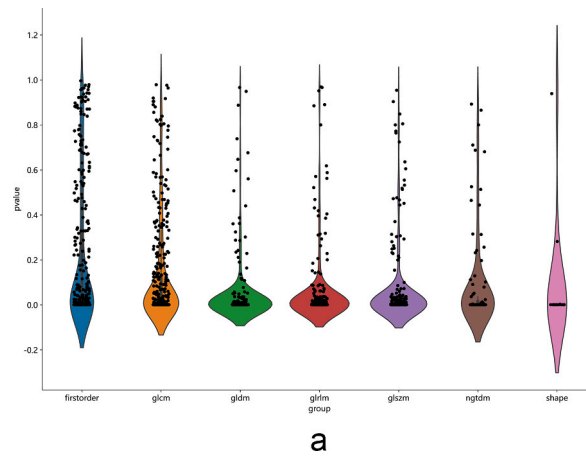**Fig. 4.** Number and proportion of handcrafted features.

Fig. 5a. All the features from the CT images and the corresponding *p*-value results.
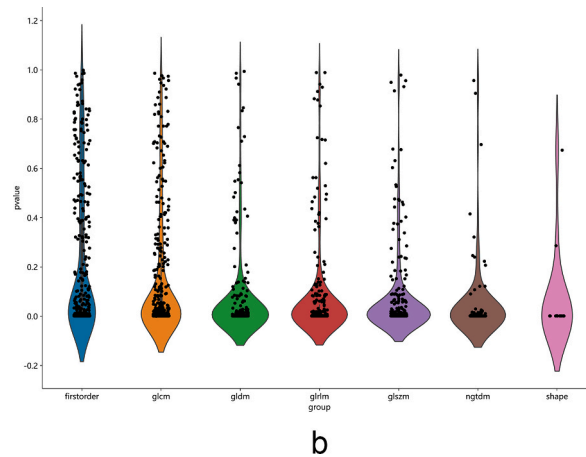

Fig. 5b. All the features from the SR-CT images and the corresponding *p*-value results.
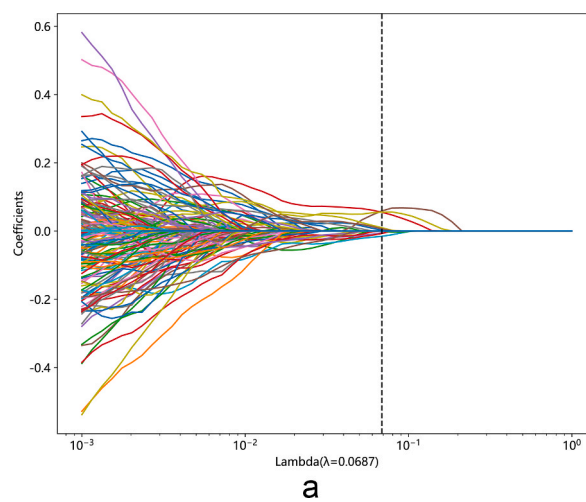

Fig. 6a. Coefficients of the 10-fold cross-validation over the CT data.
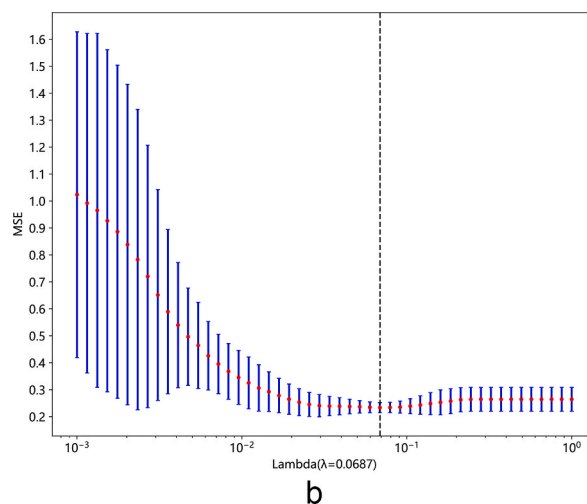
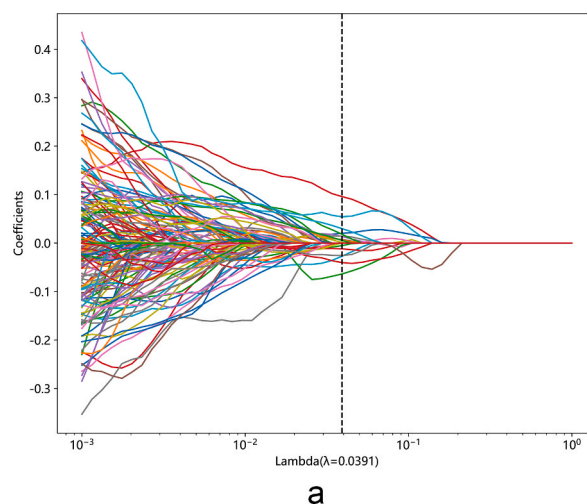**Fig. 6b.** MSE of 10-fold cross-validation over the CT data.

Fig. 7a. Coefficients of the 10-fold cross-validation over the SR-CT data.

their clinical utility. Fig. 13a and b illustrates the decision curves for the radiomics models derived from CT and SR-CT images, providing valuable insights to support clinical decision-making across a range of threshold probabilities.

Fig. 14a and b illustrates CT images alongside the corresponding pathological findings of peritumoral lung tissue in two patients diagnosed with ILA, as verified through surgical resection.

4. Discussion

We included patients with stage II or lower lung adenocarcinoma because these individuals generally have no distant metastases and predominantly receive surgical treatments [37]. On the other hand, patients with stage III or higher lung adenocarcinoma undergo more complex treatment regimes, including chemotherapy and radiotherapy. These treatments can alter imaging characteristics, affecting the model's accuracy and generalizability. By restricting our study to earlier stages of cancer, we ensure a collection of consistent, high-quality CT images and clinical data. This limitation minimizes confounding variables and establishes a robust data foundation, enhancing the precision in evaluating and validating the radiomics model [38].

Due to the significantly better prognosis of patients with microinvasive lung adenocarcinoma compared to those with more invasive forms [39], we intentionally excluded cases of microinvasive lung adenocarcinoma from our study. We also conducted a detailed review of the original pathology reports to ensure that no cases of microinvasive adenocarcinoma were included in our study cohort.

MPP and SOL components are important biomarkers for forecasting the effectiveness of adjuvant chemotherapy in lung adeno-carcinoma [40,41]. Additional research has suggested that MPP and SOL components can also guide the choice of surgical approach for
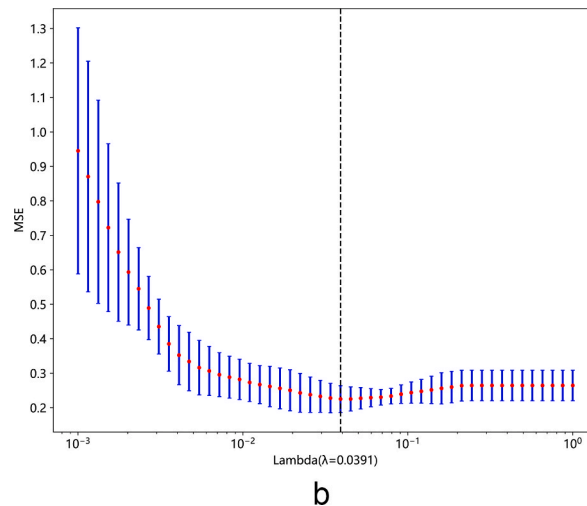
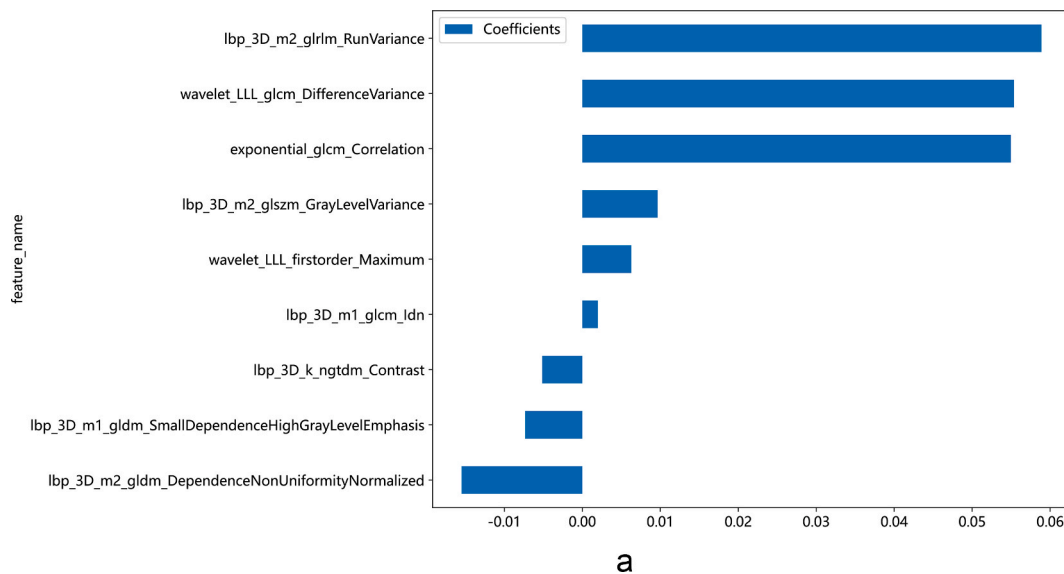**Fig. 7b.** MSE of 10-fold cross-validation over the SR-CT data.

Fig. 8a. The histogram of the rad-score based on the selected features over the CT data.

treating patients with lung adenocarcinoma. For patients with lung adenocarcinoma that includes MPP and SOL components, lobectomy may be more advisable than limited resection [13]. Intraoperative frozen section analysis, though commonly used to guide surgical decisions, has shortcomings in accurately identifying the pathological subtypes of lung adenocarcinoma. Trejo Bittar et al. investigated the agreement between frozen and paraffin-embedded sections in a study involving 112 patients with early-stage lung adenocarcinoma. They reported a concordance rate of only 69.7 %, underscoring the difficulties associated with intraoperative diagnosis of these subtypes [36]. Preservation of lung function is critically important in patients with diminished cardiopulmonary capacity, advanced age, or those needing multiple resections for multifocal lesions, thereby necessitating minimal resection of lung tissue. Consequently, detecting MPP and SOL elements in lung adenocarcinoma preoperatively is crucial for selecting the optimal surgical plan and deciding on the necessity for early aggressive adjuvant therapy. For patients who are unsuitable for surgical intervention, identifying MPP and SOL components is essential. The thorough assessment of histological subtypes necessitates the examination of the entire tumor specimen. Although the criteria for pathological subtyping are well-defined, the potential for misdiagnosis persists in clinical practice. Therefore, it is crucial to accurately identify the presence of MPP/SOL components to develop tailored treatment strategies.

Manual segmentation is crucial when precise delineation of the tumor outline, including its shape and size, is required [42]. We acknowledge that manual segmentation could introduce potential biases and affect the reproducibility of our results. To minimize these potential biases and ensure segmentation accuracy, we have implemented several measures: Initially, radiologists with over six
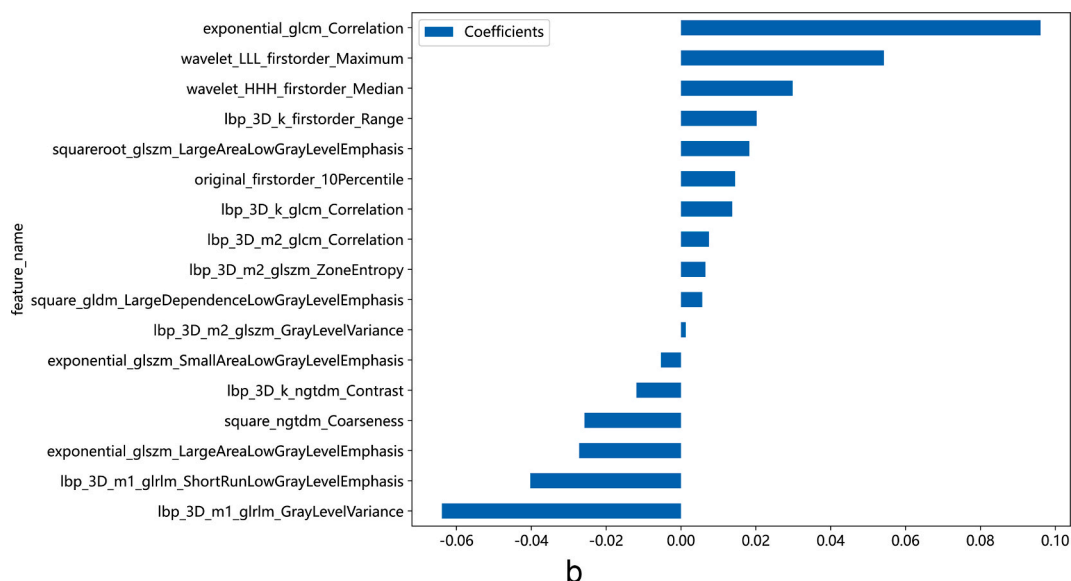
Fig. 8b. The histogram of the rad-score based on the selected features over the SR-CT data.

years of experience performed the segmentation of both CT and SR-CT images using the well-known ITK-SNAP software. Subsequently, all segmentation results underwent review and validation by a senior radiologist with 26 years of experience, ensuring high accuracy and consistency in the segmentation process. Any inconsistencies were resolved through a comprehensive discussion to reach a consensus.

While various imaging features have previously been suggested to assist in identifying different pathological subtypes and stratifying patients, these characteristics, including tumor margins and the degree of solidity, often present considerable overlap among subtypes [43]. The efficacy of classifying subtypes based on these imaging features has yet to be comprehensively assessed, and there is notable interobserver variability in their interpretation.

Initial investigations into radiomics applied to lung cancer subtypes have yielded significant insights. For example, Yang et al. demonstrated that, in a validation cohort of lung adenocarcinoma patients with high pathological purity (greater than 70 %), correctly classifying five pathological subtypes reached 83 %. In comparison, the accuracy for classifying three grades was 94 % [44]. Research by Park et al. has indicated that radiomics can distinguish between the main pathological subtypes and grades within adenocarcinomas, achieving an accuracy that is on par with the assessments conducted by radiologists [23]. Song et al. proposed that specific radiomic features, such as the minimum pixel value and the variance of positive pixel values within imaging data, could predict MPP components in lung adenocarcinoma [45]. In another study, Bae et al. differentiated various lung cancer subtypes successfully by analyzing radiomic features from dual-energy CT scans, resulting in AUC values of 0.93, 0.86, and 0.84 [46]. In our study, lung adenocarcinoma patients with less than 5 % micropapillary or solid components were categorized into the positive group to closely mirror real-world clinical conditions.

With the advent of HRCT technology capable of achieving a resolution of 150 µm, there have been significant strides in the imaging of lung adenocarcinoma. A significant study in this field successfully predicted the invasiveness of lung adenocarcinoma using CT images with a 0.25 mm slice thickness and a 2048 reconstruction matrix. The research identified two critical indicators for predicting lung cancer invasiveness: the obliteration of the air bronchogram and a solid part diameter exceeding 0.8 cm. When these two features were combined, the resulting AUC was 0.94, demonstrating a high level of diagnostic accuracy. However, a notable limitation of this high-resolution imaging technique is the associated relatively high radiation dose, with an average exposure of 8.2 mSv [47].

Deep learning super-resolution (DL-SR) technologies have garnered significant interest in medical imaging. DL-SR techniques promise to reduce the loss of high-frequency details, minimize edge blurring, and enhance overall image resolution, which is essential for improving medical image quality and diagnostic value [48,49]. Recent studies have explored how DL-SR can transform radiological analysis. For example, Fan et al. examined the effectiveness of 2D super-resolution neural networks in enhancing medical image quality and improving diagnostic accuracy [50]. Farias et al. demonstrated that super-resolution techniques based on generative adversarial networks (GANs) could strengthen the robustness of crucial radiological features, leading to more consistent and reliable imaging analysis [24]. The foundational research in this area has revealed the vast potential for DL-SR techniques in radiomics.

However, the translation of these techniques into clinical practice necessitates additional validation. D. Wessling and collaborators have effectively combined DL algorithms with SR and partial Fourier reconstruction methods to enhance the image quality and sharpness of abdominal MRI scans while simultaneously reducing breath-hold durations [51]. B. Kim and his team have applied deep learning-based imaging reconstruction techniques for evaluating rectal cancer post-radiochemotherapy, significantly enhancing MRI image quality and diagnostic accuracy for complete pathological remission [52]. J.A. Steeden and others developed a rapid whole-heart CMR technique utilizing residual U-Net for super-resolution reconstruction. This effectively restores high-resolution

Table 2

The optimal model was obtained by using rad features compared with an LR, SVM, KNN, Random Forest, Extra Trees, XGBoost, LightGBM, and MLP classifier. SVM achieved the best value of AUC in the train and test cohort reached 0.864 and 0.761 , respectively.

| model_name	Accuracy	AUC	95 % CI	Sensitivity	Specificity	PPV	NPV	Precision	Recall	F1	Threshold	Task
LR	0.731	0.804	0.7391–0.8688	0.662	0.787	0.718	0.740	0.718	0.662	0.689	0.480	label-train
LR	0.676	0.749	0.6309–0.8665	0.606	0.732	0.645	0.698	0.645	0.606	0.625	0.641	label-test
SVM	0.754	0.864	0.8107–0.9179	0.649	0.840	0.769	0.745	0.769	0.649	0.704	0.261	label-train
SVM	0.689	0.761	0.6503–0.8707	0.636	0.732	0.656	0.714	0.656	0.636	0.646	0.553	label-test
KNN	0.749	0.816	0.7556–0.8766	0.727	0.766	0.718	0.774	0.718	0.727	0.723	0.600	label-train
KNN	0.649	0.686	0.5623–0.8087	0.636	0.659	0.600	0.692	0.600	0.636	0.618	0.600	label-test
RandomForest	0.965	0.999	0.9974–1.0000	0.922	1.000	1.000	0.940	1.000	0.922	0.959	0.500	label-train
RandomForest	0.662	0.682	0.5554–0.8083	0.576	0.732	0.633	0.682	0.633	0.576	0.603	0.600	label-test
ExtraTrees	1.000	1.000	1.0000–1.0000	1.000	1.000	1.000	1.000	1.000	1.000	1.000	1.000	label-train
ExtraTrees	0.676	0.665	0.5371–0.7933	0.455	0.854	0.714	0.660	0.714	0.455	0.556	0.600	label-test
XGBoost	0.994	1.000	0.9991–1.0000	1.000	0.989	0.987	1.000	0.987	1.000	0.994	0.540	label-train
XGBoost	0.649	0.689	0.5623–0.8161	0.576	0.707	0.613	0.674	0.613	0.576	0.594	0.564	label-test
LightGBM	0.789	0.900	0.8559–0.9438	0.688	0.872	0.815	0.774	0.815	0.688	0.746	0.471	label-train
LightGBM	0.676	0.731	0.6122–0.8504	0.576	0.756	0.655	0.689	0.655	0.576	0.613	0.587	label-test
MLP	0.743	0.805	0.7394–0.8696	0.636	0.830	0.754	0.736	0.754	0.636	0.690	0.483	label-train
MLP	0.703	0.752	0.6335–0.8713	0.576	0.805	0.704	0.702	0.704	0.576	0.633	0.677	label-test
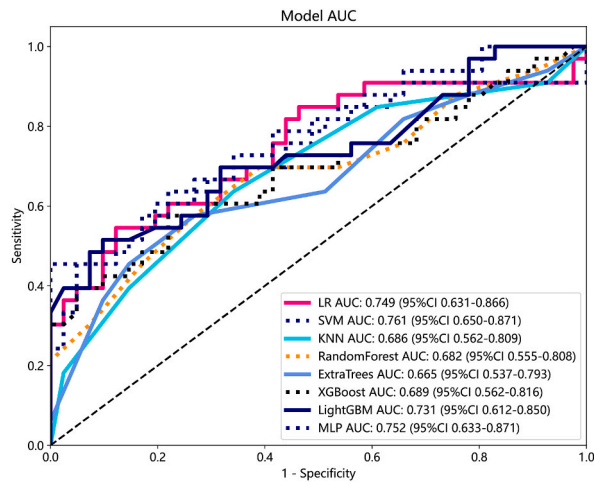
Fig. 9. The AUC of each radiomics model on the CT test cohort.
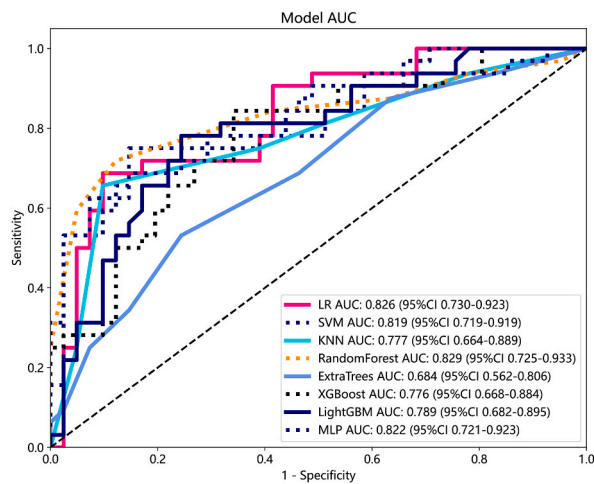

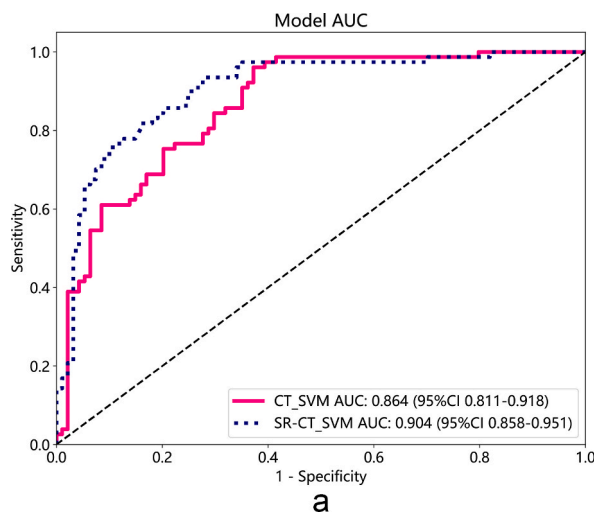**Fig. 10.** The AUC of each radiomics model on the SR-CT test cohort.

Fig. 11a. The comparison of the AUC for SVM models of CT radiomics and SR-CT radiomics in the training cohorts.
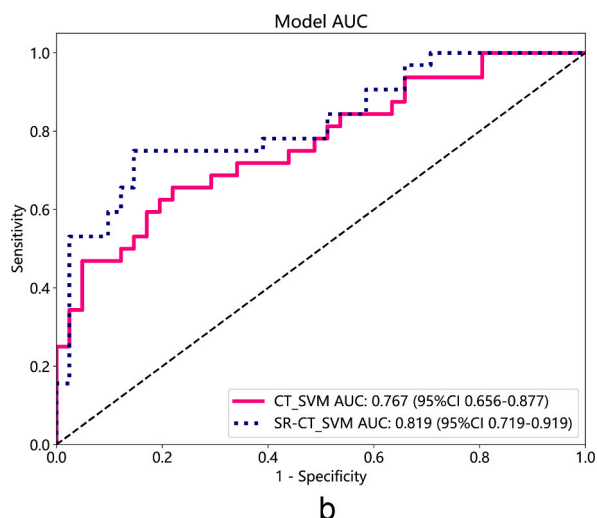
Fig. 11b. The comparison of the AUC for SVM models of CT radiomics and SR-CT radiomics in the test cohorts.

features and boosts diagnostic confidence, all while markedly shortening scanning times [53]. S. Dencks and partners implemented super-resolution ultrasound imaging to detect breast cancer, proving its feasibility and efficacy in this application [54]. R.R. Sood and his team improved image resolution and registration accuracy using super-resolution volumetric reconstruction for preoperative prostate MRI and histopathological image registration, contributing to precise prostate cancer diagnosis and treatment planning [55].

Our current study has advanced beyond prior work by developing a GAN-based SR-CT model, specifically focusing on its clinical application for predicting MPP and SOL components within lung adenocarcinoma. Our study demonstrated that the SR-CT model, enhanced by DL techniques, outperformed the conventional CT model regarding diagnostic accuracy. Specifically, in the training and test cohorts, the SR-CT model recorded AUC values of 0.904 and 0.819, respectively. This enhancement is likely due to the DL-SR method's capacity to provide more detailed information through precise interpolation, enabling a more sensitive radiomic analysis to discern nuanced morphological and pathophysiological tumor changes.

SR reconstruction technology, while offering significant advantages, also has certain limitations. This technique, which enhances image resolution through algorithms, may introduce reconstruction errors, particularly in handling image edges and details. Moreover, it is essential to recognize that the quality of SR images fundamentally relies on the quality of the original CT images. Poor-quality original images can adversely affect the quality of SR images, which can subsequently impact the reliability of radiomic analysis. The utilization of this technology is further constrained by differences in scanning equipment and operational protocols between institutions, which can affect the consistency and reproducibility of images, limiting their broader application. SR technology typically requires high computational resources and processing time, which may pose a barrier in emergency clinical settings. Moreover, enhanced images may display non-traditional visual features, requiring additional training for radiologists to interpret accurately [56, 57]. Therefore, it is necessary to conduct more extensive clinical trials to further validate the effectiveness and feasibility of SR technology in actual clinical applications.

Moreover, the GAN model itself is a highly intricate and non-linear system, which underscores the importance of your work. Its sensitivity to initial parameters and randomness during training can lead to fluctuations in the calibration curves, even if the model performs well in the training cohort. Unseen data distributions or features in the test cohort can significantly impact the model's performance, necessitating adjustments and optimizations of model parameters during training [58,59].

Our study incorporated data from six models of CT machines produced by four different manufacturers, enhancing our dataset's representativeness and diversity and consequently improving our findings' reliability. We introduced innovative techniques such as super-resolution image technology and multiple machine learning algorithms, which have significantly advanced the accuracy of predicting the histological structure of lung adenocarcinoma. Various machine learning classifiers were selected based on their extensive utilization in medical image processing and their proven effectiveness in prior research [60–63]. For instance, SVM was chosen for its exceptional performance with high-dimensional data [64]. Moreover, we favored tree-based models, including Random Forest, XGBoost, and LightGBM, due to their proficiency in handling intricate data structures [65,66]. We conducted systematic hyperparameter tuning for each model, primarily using grid search combined with cross-validation to ensure optimal performance and prevent overfitting [67,68]. In addition, data normalization was performed to ensure better stability and efficiency in the training process. Our objective was to determine the most effective model by evaluating the performance of various algorithms on our research dataset. Upon assessing the AUC scores and other performance metrics, including precision and recall, we observed that SVM consistently outperformed other models, leading us to select it as the final model.

A Rad-score is a composite quantitative measure that amalgamates various radiomic features derived from computational models like linear regression to reflect a tumor's biological properties accurately. Offering a higher predictive accuracy, a Rad-score significantly augments the prediction of tumor behavior, which is vital for clinical practice. It assists in diagnosis and prognostication and

Table 3
Predictive performance of CT and SR-CT radiomics.

| Signature	Accuracy	AUC	95 % CI	Sensitivity	Specificity	PPV	NPV	Precision	Recall	F1	Threshold	Cohort
CT_SVM	0.754	0.864	0.8107–0.9179	0.649	0.840	0.769	0.745	0.769	0.649	0.704	0.261	Train
SR-CT_SVM	0.819	0.904	0.8579–0.9506	0.779	0.851	0.811	0.825	0.811	0.779	0.795	0.546	Train
CT_SVM	0.699	0.767	0.6561–0.8775	0.656	0.732	0.656	0.732	0.656	0.656	0.656	0.553	Test
SR-CT_SVM	0.781	0.819	0.7194–0.9193	0.750	0.805	0.750	0.805	0.750	0.750	0.750	0.518	Test
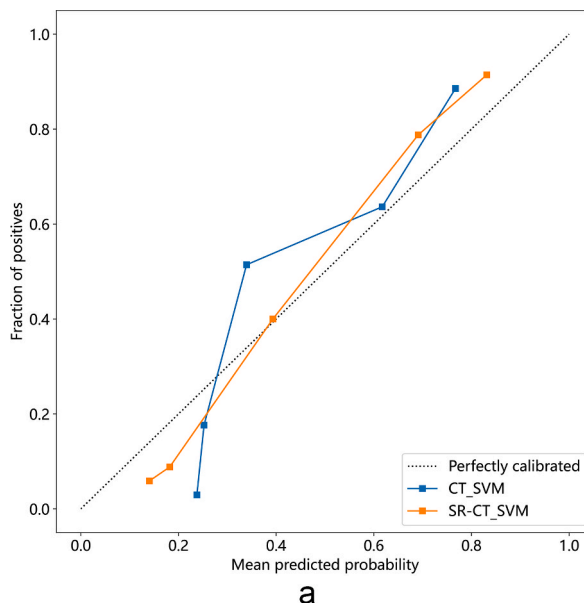
Fig. 12a. The calibration curves in the train and test cohort over CT and SR-CT data. Calibration curves are presented based on two models for predicting the micropapillary and solid components of invasive lung adenocarcinoma. The x-axis represents the predicted micropapillary and solid components probabilities based on the radiomics signature. At the same time, displays the actual probabilities of these components. The 45° diagonal line symbolizes the ideal prediction, with the blue, yellow lines representing the predictive performance of the CT radiomics and SR-CT radiomics, respectively. Fig. 12a: Comparison of the calibration curves for CT and SR-CT radiomics in the training cohorts. The calibration curves demonstrated good calibration of the models in both cohorts.
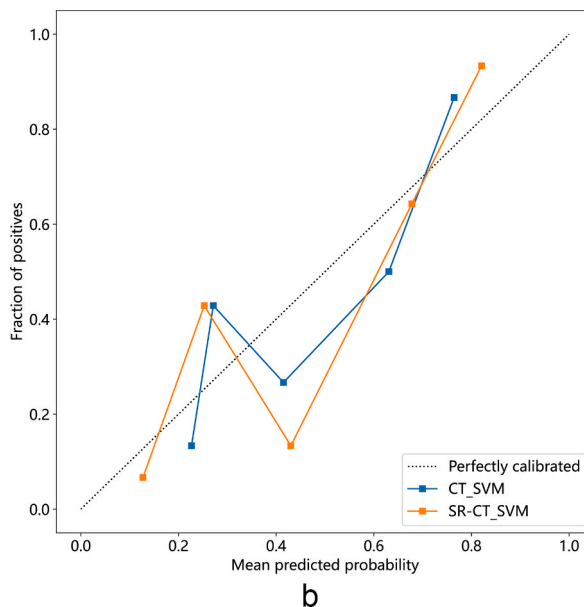

Fig. 12b. Comparison of the calibration curves for CT and SR-CT radiomics in the test cohorts in both cohorts. The calibration curves demonstrated good calibration of the models in both cohorts.

serves as a foundation for formulating personalized treatment strategies. Furthermore, Rad-score exposes a link between the heterogeneity exhibited by tumors in CT imaging and their potential for invasiveness and unfavorable prognosis [69]. These findings provide a valuable tool for more accurately predicting the clinical progression of lung cancer in patients, enabling the development of more targeted and effective treatment strategies.

Patients can be stratified into risk categories based on the model's predictions [70,71]. Those identified with a high likelihood of having MPP/SOL components can be flagged for more aggressive or tailored treatment plans. The predictive information can assist
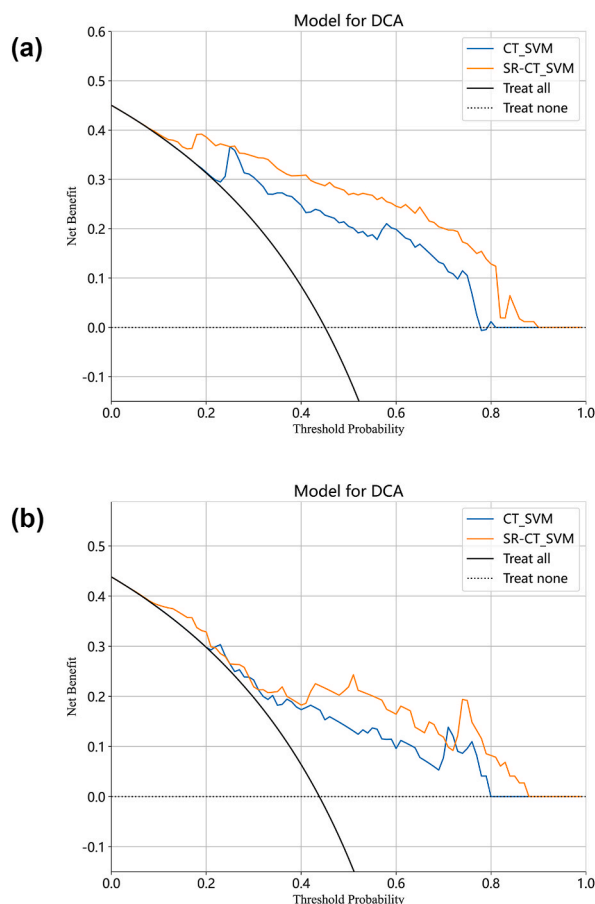
Fig. 13. The DCA curves in the training and test cohort over CT and SR-CT data. The x-axis delineates the threshold probability, while the y-axis quantifies the net benefit. The black line represents the assumption that no patients with invasive lung adenocarcinoma have micropapillary and solid components. In the training cohort (A) and the test cohort (B), the DCA curve of the SVM model for SR-CT radiomics is higher than that for CT radiomics, indicating that the SVM model for SR-CT radiomics can provide a more significant net benefit than the SVM model for CT radiomics.

clinicians in making better-informed decisions about the need for further preoperative investigations, potential adjustments to surgical techniques, and the consideration of adjuvant therapies following surgery [72].

The training cohort and test cohort may differ in sample size and sample distribution, particularly in the distribution of key features. This can lead to inconsistencies in the model's performance across different datasets, resulting in fluctuations in the calibration curves. The test cohort may include features or noise absent in the training cohort, potentially impacting the model's predictive performance and causing fluctuations in the calibration curve [73,74].

This study presents several limitations. The retrospective, single-center design may introduce selection bias, potentially affecting the generalizability of the results. To address potential confounding factors, future studies should adopt a prospective, multicenter approach. Such studies would also allow rigorous testing of the model's stability and practical applicability across various clinical settings. Second, the radiomics model's reliance on manually delineated regions introduced additional complexity to the segmentation process, which was further amplified by using fourfold super-resolution reconstruction techniques. Future research could incorporate automated segmentation processes, which may identify more discriminating features when combined with radiomic analysis and DL. This integration promises to streamline the workflow and enhance the robustness of super-resolution reconstruction methods in medical imaging. Lastly, determining the most effective model remains an open question requiring additional investigation. Future research directions include increasing the sample size to enhance statistical power and integrating more sophisticated technological advancements to refine radiological diagnostic accuracy further.

5. Conclusion

The study successfully established and verified a DL-enhanced SR-CT radiomics model. This model outperformed conventional CT radiomics models in predicting MPP/SOL patterns in lung adenocarcinoma. Continued research and broader validation are necessary to fully harness and refine the clinical potential of radiomics when combined with super-resolution reconstruction technology.
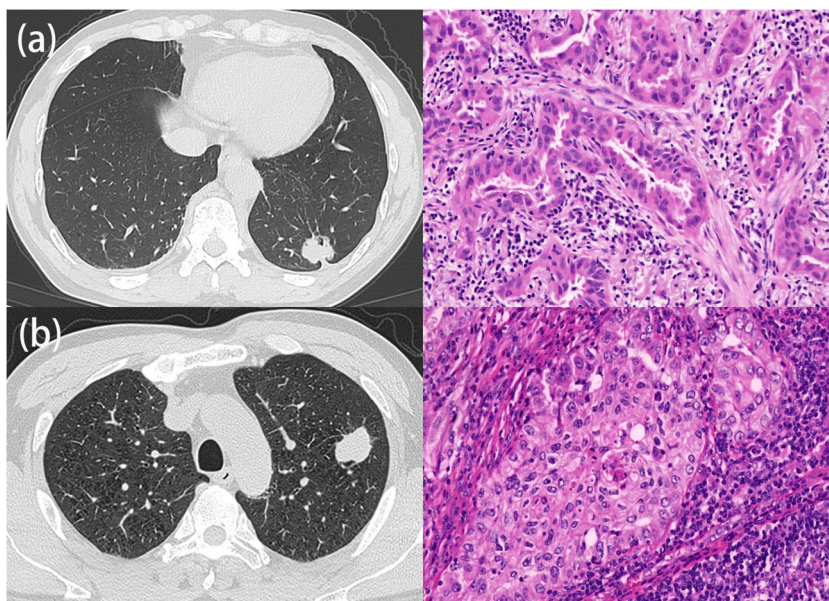
Fig. 14. CT images and corresponding pathology of peripheral invasive lung adenocarcinoma in two patients: (a) A 64-year-old woman with a diagnosis of invasive lung adenocarcinoma. CT shows a solid nodule in the lower lobe of the left lung, with a diameter of 25 mm. High-power histologic image (hematoxylin and eosin, × 200) shows that the tumor has irregular glandular-like structures, abundant eosinophilic cytoplasm, and significant cellular atypia. The primary pathological type is acinar, accompanied by papillary structures. The SR-CT radiomics SVM model predicts a probability of 0.24 for containing MPP/SOL components. (b) A 60-year-old man with a diagnosis of invasive lung adenocarcinoma. CT shows a solid nodule in the upper lobe of the left lung, with a diameter of 27 mm. High-power histologic image (hematoxylin and eosin, × 200) shows that the tumor appears as solid sheets with cells of varying sizes and significant pleomorphism. The cytoplasm is abundant, with some cells displaying clear cytoplasm and visible nucleoli. Nuclear division is also observed. The stroma shows substantial infiltration of inflammatory cells. The final pathological classification is 40 % micropapillary, 14 % solid, and 11 % papillary. The SR-CT radiomics SVM model predicts a probability of 0.76 for containing MPP/SOL components. SR-CT, super-resolution CT; SVM, Support Vector Machines; MPP, micropapillary; SOL, solid.

Ethics statement

This study protocol received approval from the Ethics Committee of Zhejiang Hospital (approval number 2023-37K). The study was conducted by the principles outlined in the Declaration of Helsinki. The authors accept full responsibility for every aspect of the work, guaranteeing that questions regarding the accuracy or integrity of any part of the study are carefully investigated and resolved.

Data availability

Due to patient privacy concerns and data confidentiality agreements, our experimental data have not been publicly available. However, the datasets used in this study can be obtained from the corresponding author upon reasonable request.

CRediT authorship contribution statement

Xiaowei Xing: Writing – original draft. **Liangping Li:** Investigation. **Mingxia Sun:** Data curation. **Jiahu Yang:** Visualization, Validation. **Xinhai Zhu:** Software, Funding acquisition, Formal analysis. **Fang Peng:** Writing – original draft. **Jianzong Du:** Supervision. **Yue Feng:** Writing – review & editing, Conceptualization.

Declaration of competing interest

The authors declare the following financial interests/personal relationships which may be considered as potential competing interests:Xinhai Zhu reports article publishing charges was provided by Zhejiang Medicine and Health Science and Technology Project. If there are other authors, they declare that they have no known competing financial interests or personal relationships that could have appeared to influence the work reported in this paper.

Acknowledgments

References

[1] H. Sung, et al., Global cancer statistics 2020: GLOBOCAN estimates of incidence and mortality worldwide for 36 cancers in 185 countries, CA A Cancer J. Clin. 71 (3) (2021) 209–249.

[2] W.D. Travis, et al., International Association for the Study of Lung Cancer/American Thoracic Society/European Respiratory Society International multidisciplinary classification of lung adenocarcinoma, J. Thorac. Oncol. 6 (2) (2011) 244–285.

[3] P.A. Russell, et al., Does lung adenocarcinoma subtype predict patient survival?: a clinicopathologic study based on the New International Association for the Study of Lung Cancer/American Thoracic Society/European Respiratory Society International multidisciplinary lung adenocarcinoma classification, J. Thorac. Oncol. 6 (9) (2011) 1496–1504.

[4] A. Yoshizawa, et al., Impact of proposed IASLC/ATS/ERS classification of lung adenocarcinoma: prognostic subgroups and implications for further revision of staging based on analysis of 514 stage I cases, Mod. Pathol. 24 (5) (2011) 653–664.

[5] Y. Cao, et al., Clinical impacts of a micropapillary pattern in lung adenocarcinoma: a review, OncoTargets Ther. 9 (2016) 149–158.

[6] J.E. Leeman, et al., Histologic subtype in core lung biopsies of early-stage lung adenocarcinoma is a prognostic factor for treatment response and failure patterns after stereotactic body radiation therapy, Int. J. Radiat. Oncol. Biol. Phys. 97 (1) (2017) 138–145.

[7] F. Qian, et al., Prognostic significance and adjuvant chemotherapy survival benefits of a solid or micropapillary pattern in patients with resected stage IB lung adenocarcinoma, J. Thorac. Cardiovasc. Surg. 155 (3) (2018) 1227–1235 e2.

[8] G. Lee, et al., Clinical impact of minimal micropapillary pattern in invasive lung adenocarcinoma, Am. J. Surg. Pathol. 39 (5) (2015) 660–666.

[9] Y. Wang, et al., Predictors of recurrence and survival of pathological T1N0M0 invasive adenocarcinoma following lobectomy, J. Cancer Res. Clin. Oncol. 144 (6) (2018) 1015–1023.

[10] K.J. Butnor, Controversies and challenges in the histologic subtyping of lung adenocarcinoma, Transl. Lung Cancer Res. 9 (3) (2020) 839–846.

[11] M.J. Cha, et al., Micropapillary and solid subtypes of invasive lung adenocarcinoma: clinical predictors of histopathology and outcome, J. Thorac. Cardiovasc. Surg. 147 (3) (2014) 921–928 e2.

[12] Y. Zhao, et al., Minor components of micropapillary and solid subtypes in lung adenocarcinoma are predictors of lymph node metastasis and poor prognosis, Ann. Surg Oncol. 23 (6) (2016) 2099–2105.

[13] J.-i. Nitadori, et al., Impact of micropapillary histologic subtype in selecting limited resection vs lobectomy for lung adenocarcinoma of 2cm or smaller, JNCI: J. Natl. Cancer Inst. 105 (16) (2013) 1212–1220.

[14] J.-J. Hung, et al., Prognostic factors of survival after recurrence in patients with resected lung adenocarcinoma, J. Thorac. Oncol. 10 (9) (2015) 1328–1336.

[15] K.-Y. Huang, et al., Inaccuracy of lung adenocarcinoma subtyping using preoperative biopsy specimens, J. Thorac. Cardiovasc. Surg. 154 (1) (2017) 332–339.e1.

[16] P.C. Tsai, et al., CT-guided core biopsy for peripheral sub-solid pulmonary nodules to predict predominant histological and aggressive subtypes of lung adenocarcinoma, Ann. Surg Oncol. 27 (11) (2020) 4405–4412.

[17] P. Lambin, et al., Radiomics: extracting more information from medical images using advanced feature analysis, Eur. J. Cancer 48 (4) (2012) 441–446.

[18] R.J. Gillies, P.E. Kinahan, H. Hricak, Radiomics: images are more than pictures, they are data, Radiology 278 (2) (2016) 563–577.

[19] M. Khorrami, et al., Stable and discriminating radiomic predictor of recurrence in early stage non-small cell lung cancer: multi-site study, Lung Cancer 142 (2020) 90–97.

[20] J. Zheng, et al., Development of a noninvasive tool to preoperatively evaluate the muscular invasiveness of bladder cancer using a radiomics approach, Cancer 125 (24) (2019) 4388–4398.

[21] V. Kumar, et al., Radiomics: the process and the challenges, Magn. Reson. Imag. 30 (9) (2012) 1234–1248.

[22] L.W. Chen, et al., Prediction of micropapillary and solid pattern in lung adenocarcinoma using radiomic values extracted from near-pure histopathological subtypes, Eur. Radiol. 31 (7) (2021) 5127–5138.

[23] S. Park, et al., Differentiation of predominant subtypes of lung adenocarcinoma using a quantitative radiomics approach on CT, Eur. Radiol. 30 (9) (2020) 4883–4892.

[24] E.C. de Farias, et al., Impact of GAN-based lesion-focused medical image super-resolution on the robustness of radiomic features, Sci. Rep. 11 (1) (2021) 21361.

[25] E. Van Reeth, et al., Super-resolution in magnetic resonance imaging: a review, Concepts Magn. Reson. 40 (6) (2012) 306–325.

[26] K. Singh, M. Saxena, M.T. Scholar, A review on medical image super resolution with application of deep learning, Smart Moves Journal Ijoscience 7 (2021) 25–29.

[27] S. Park, et al., Computer-aided detection of subsolid nodules at chest CT: improved performance with deep learning–based CT section thickness reduction, Radiology 299 (1) (2021) 211–219.

[28] M. Hou, L. Zhou, J. Sun, Deep-learning-based 3D super-resolution MRI radiomics model: superior predictive performance in preoperative T-staging of rectal cancer, Eur. Radiol. 33 (1) (2023) 1–10.

[29] H.J. Aerts, et al., Decoding tumour phenotype by noninvasive imaging using a quantitative radiomics approach, Nat. Commun. 5 (1) (2014) 4006.

[30] J.J.M. van Griethuysen, et al., Computational radiomics system to decode the radiographic phenotype, Cancer Res. 77 (21) (2017) e104–e107.

[31] Y.-C. Heo, K. Kim, Y. Lee, Image denoising using non-local means (NLM) approach in magnetic resonance (MR) imaging: a systematic review, Appl. Sci. 10 (20) (2020) 7028.

[32] M. Ragusi, et al., Evaluation of CT angiography image quality acquired with single-energy metal artifact reduction (SEMAR) algorithm in patients after complex endovascular aortic repair, Cardiovasc. Intervent. Radiol. 41 (2) (2018) 323–329.

[33] H.W. Herwanto, et al., Comparison of min-max, z-score and decimal scaling normalization for zoning feature extraction on Javanese character recognition, in: 2021 7th International Conference on Electrical, Electronics and Information Engineering (ICEEIE), IEEE, 2021.

[34] C. Yang, et al., Prediction of metastasis in the axillary lymph nodes of patients with breast cancer: a radiomics method based on contrast-enhanced computed tomography, Front. Oncol. 11 (2021) 726240.

[35] J.M. Wolterink, et al., Generative adversarial networks: a primer for radiologists, Radiographics 41 (3) (2021) 840–857.

[36] H.E. Trejo Bittar, et al., Accuracy of the IASLC/ATS/ERS histological subtyping of stage I lung adenocarcinoma on intraoperative frozen sections, Mod. Pathol. 28 (8) (2015) 1058–1063.

[37] A.K. Ganti, et al., Update of incidence, prevalence, survival, and initial treatment in patients with non-small cell lung cancer in the US, JAMA Oncol. 7 (12) (2021) 1824–1832.

[38] S.S. Yip, H.J. Aerts, Applications and limitations of radiomics, Phys. Med. Biol. 61 (13) (2016) R150–R166.

[39] M. Yotsukura, et al., Long-term prognosis of patients with resected adenocarcinoma in situ and minimally invasive adenocarcinoma of the lung, J. Thorac. Oncol. 16 (8) (2021) 1312–1320.

[40] C. Wang, J. Yang, M. Lu, Micropapillary predominant lung adenocarcinoma in stage IA benefits from adjuvant chemotherapy, Ann. Surg Oncol. 27 (6) (2020) 2051–2060.

[41] J.-J. Hung, et al., Adjuvant chemotherapy improves the probability of freedom from recurrence in patients with resected stage IB lung adenocarcinoma, Ann. Thorac. Surg. 101 (4) (2016) 1346–1353.

[42] C. Hassani, et al., Radiomics in pulmonary lesion imaging, AJR Am. J. Roentgenol. 212 (3) (2019) 497–504.

[43] M. Lederlin, et al., Correlation of radio- and histomorphological pattern of pulmonary adenocarcinoma, Eur. Respir. J. 41 (4) (2013) 943–951.

[44] S.M. Yang, et al., Extraction of radiomic values from lung adenocarcinoma with near-pure subtypes in the International Association for the Study of Lung Cancer/the American Thoracic Society/the European Respiratory Society (IASLC/ATS/ERS) classification, Lung Cancer 119 (2018) 56–63.

[45] S.H. Song, et al., Imaging phenotyping using radiomics to predict micropapillary pattern within lung adenocarcinoma, J. Thorac. Oncol. 12 (4) (2017) 624–632.

[46] J.M. Bae, et al., Pathologic stratification of operable lung adenocarcinoma using radiomics features extracted from dual energy CT images, Oncotarget 8 (1) (2017) 523–535.

[47] M. Yanagawa, et al., Lung adenocarcinoma at CT with 0.25-mm section thickness and a 2048 matrix: high-spatial-resolution imaging for predicting invasiveness, Radiology 297 (2) (2020) 462–471.

[48] C. Ma, et al., Learning a no-reference quality metric for single-image super-resolution, Comput. Vis. Image Understand. 158 (2017) 1–16.

[49] W. Yang, et al., Deep learning for single image super-resolution: a brief review, IEEE Trans. Multimed. 21 (12) (2019) 3106–3121.

[50] M. Fan, et al., Generative adversarial network-based super-resolution of diffusion-weighted imaging: application to tumour radiomics in breast cancer, NMR Biomed. 33 (8) (2020) e4345.

[51] D. Wessling, et al., Application of a deep learning algorithm for combined super-resolution and partial Fourier reconstruction including time reduction in T1-weighted precontrast and postcontrast gradient echo imaging of abdominopelvic MR imaging, Diagnostics 12 (10) (2022).

[52] B. Kim, et al., Deep learning-based imaging reconstruction for MRI after neoadjuvant chemoradiotherapy for rectal cancer: effects on image quality and assessment of treatment response, Abdom Radiol (NY) 48 (1) (2023) 201–210.

[53] J.A. Steeden, et al., Rapid whole-heart CMR with single volume super-resolution, J. Cardiovasc. Magn. Reson. 22 (1) (2020) 56.

[54] S. Dencks, et al., Clinical pilot application of super-resolution US imaging in breast cancer, IEEE Trans. Ultrason. Ferroelectrics Freq. Control 66 (3) (2019) 517–526.

[55] R.R. Sood, et al., 3D Registration of pre-surgical prostate MRI and histopathology images via super-resolution volume reconstruction, Med. Image Anal. 69 (2021) 101957.

[56] Y. Li, B. Sixou, F. Peyrin, A review of the deep learning methods for medical images super resolution problems, Irbm 42 (2) (2021) 120–133.

[57] S. Umirzakova, et al., Enhancing the super-resolution of medical images: introducing the deep residual feature distillation channel attention network for optimized performance and efficiency, Bioengineering 10 (11) (2023).

[58] S. Gbashi, et al., Application of a generative adversarial network for multi-featured fermentation data synthesis and artificial neural network (ANN) modeling of bitter gourd-grape beverage production, Sci. Rep. 13 (1) (2023) 11755.

[59] G. Heilemann, et al., Can Generative Adversarial Networks help to overcome the limited data problem in segmentation? Z. Med. Phys. 32 (3) (2022) 361–368.

[60] S. Hussain, et al., Deep learning, radiomics and radiogenomics applications in the digital breast tomosynthesis: a systematic review, BMC Bioinf. 24 (1) (2023) 401.

[61] S. Li, et al., A comprehensive review on radiomics and deep learning for nasopharyngeal carcinoma imaging, Diagnostics 11 (9) (2021).

[62] Q. Lin, et al., CT-based radiomics in predicting pathological response in non-small cell lung cancer patients receiving neoadjuvant immunotherapy, Front. Oncol. 12 (2022) 937277.

[63] C.Y. Xie, et al., Machine learning and radiomics applications in esophageal cancers using non-invasive imaging methods-A critical review of literature, Cancers 13 (10) (2021).

[64] A. Roy, S. Chakraborty, Support vector machine in structural reliability analysis: a review, Reliab. Eng. Syst. Saf. 233 (2023) 109126.

[65] N. Donges, M. Urwin, S. Pierre, Random Forest: a complete guide for machine learning, 2023. Built In (2023). [Online]. Available: on the World Wide Web: https://builtin.com/data-science/random-forest-algorithm#procon.

[66] M. Banerjee, et al., Tree-based analysis: a practical approach to create clinical decision-making tools, Circulation: Cardiovascular Quality and Outcomes 12 (5) (2019) e004879.

[67] M. Adnan, et al., Utilizing grid search cross-validation with adaptive boosting for augmenting performance of machine learning models, PeerJ Comput Sci 8 (2022) e803.

[68] S.F.M. Radzi, et al., Hyperparameter tuning and pipeline optimization via grid search method and tree-based AutoML in breast cancer prediction, J. Personalized Med. 11 (10) (2021).

[69] S.Y. Park, et al., Imaging heterogeneity in lung cancer: techniques, applications, and challenges, Am. J. Roentgenol. 207 (3) (2016) 534–543.

[70] M. Bhagawati, et al., Cardiovascular disease/stroke risk stratification in deep learning framework: a review, Cardiovasc. Diagn. Ther. 13 (3) (2023) 557–598.

[71] X. Shu, et al., Radiomic-based machine learning model for the accurate prediction of prostate cancer risk stratification, Br. J. Radiol. 96 (1143) (2023) 20220238.

[72] T. Wang, et al., Radiomics for survival risk stratification of clinical and pathologic stage IA pure-solid non-small cell lung cancer, Radiology 302 (2) (2022) 425–434.

[73] Y. Kawazoe, et al., Comparison of the radiomics-based predictive models using machine learning and nomogram for epidermal growth factor receptor mutation status and subtypes in lung adenocarcinoma, Phys Eng Sci Med 46 (1) (2023) 395–403.

[74] J. Xiao, et al., The application and comparison of machine learning models for the prediction of breast cancer prognosis: retrospective cohort study, JMIR Med Inform 10 (2) (2022) e33440.